

# Raman Scattering as a Selective Probe of Chiral Electronic Excitations in Bilayer Graphene

E Riccardi<sup>1‡</sup>, O Kashuba<sup>2</sup>, M Cazayous<sup>1</sup>, A Sacuto<sup>1</sup> and Y Gallais<sup>1</sup>

<sup>1</sup>Laboratoire Matériaux et Phénomènes Quantiques (UMR 7162 CNRS), Université Paris Diderot-Paris 7, Bâtiment Condorcet, 75205 Paris Cedex 13, FR

<sup>2</sup> Department of Theoretical Physics and Astrophysics, University of Würzburg, Am Hubland, D-97074 Würzburg, Germany

E-mail: elisa.riccardi@lpa.ens.fr, yann.gallais@paris7.jussieu.fr, okashuba@physik.uni-wuerzburg.de

May 2018

**Abstract.** We report a symmetry resolved electronic Raman scattering (ERS) study of a bilayer graphene device under gate voltage. We show that the ERS continuum is dominated by interband chiral excitations of  $A_2$  symmetry and displays a characteristic Pauli-blocking behavior similar to the monolayer case. Crucially, we show that non-chiral excitations make a vanishing contribution to the Raman cross-section due to destructive interference effects in the Raman amplitude matrix elements. This is in a marked contrast to optical absorption measurements and opens interesting venues for the use of Raman scattering as a selective probe of chiral degrees of freedom in topological matter and other 2D crystals.

*Keywords:* Bilayer Graphene, Electronic Raman Spectroscopy, Gate Tuning, chirality, isospin

‡ Present address: Laboratoire Pierre Aigrain, ENS, 24 rue Lhomond, 75005 Paris

## 1. Introduction

Monolayer graphene exhibits an unique low energy electronic structure with Dirac-like linear bands. This structure has important consequences on the properties of electrons and holes: monolayer graphene electrons can be described as massless relativistic particles. Dirac electrons in graphene have a chiral nature, which has profound consequences on the transport properties of Dirac electrons through potential barriers, i.e. the so-called Klein tunneling [1]. In monolayer graphene, the chirality phenomenon is linked to the existence of two inequivalent sub-lattice carbon sites which act as isospin degrees of freedom [2, 3]. Historically this chirality is defined as the projection of the isospin on the direction of momentum, a property, which in the particle physics language is called helicity (see Appendix 1 for a discussion of the distinction between chirality and helicity in the context of graphene). Interestingly, chirality can also be defined for the low energy massive Dirac electrons in bilayer graphene. Here, in contrast to monolayer graphene, the chiral nature of the low energy electrons is not related to sub-lattice degree of freedom, but to the layer index, which can also act as an isospin degree of freedom [4, 5, 6]. The chiral nature of electrons in graphene systems is shared by topological insulators, where strong spin-orbit coupling leads to spin-momentum locking of Dirac particles [7]. The chiral spin-textures at the surface of the topological insulator  $\text{Bi}_2\text{Se}_3$  have been successfully probed by spin-resolved Angle Resolved Photoemission Electron Spectroscopy measurements [8, 9, 10], and their associated collective chiral excitations has been recently revealed by Raman spectroscopy [11].

Since chiral phenomenon is associated with isospin instead of the real spin, probing chirality and isospin excitations in graphene-like systems has proven somewhat more elusive. To this end, electronic Raman scattering (ERS) has recently proven to be a powerful tool to study electronic excitations in graphene. In particular, while initial studies were focused on inter-Landau level excitations under strong magnetic field [12, 13, 14], it was recently shown by polarization resolved measurements that the ERS continuum at zero magnetic field is dominated by interband chiral excitations across the Dirac point [15]. Here we use a common terminology, where “chiral” Raman excitation means the Raman-excited electron-hole pair, where electron and hole have the opposite chiralities. As predicted theoretically [16], these excitations display Pauli-blocking behavior upon tuning the Fermi level with a gate voltage. However, due to its simple band structure, the only available vertical interband transitions in monolayer graphene are chiral and the ERS spectrum of these interband excitations does not differ significantly from the well-studied infrared absorption spectra [17]. By contrast, in absorption experiments, bilayer graphene displays a much richer spectrum of excitations with only a sub-set of them having chiral character, providing an appealing platform to demonstrate the selectivity of polarization resolved ERS measurements with respect to conventional infrared transmission measurements.

In this paper we demonstrate this selectivity by studying ERS in a bilayer graphene device. We first show theoretically that the dominant ERS processes correspond to

excitations belonging the  $A_2$  representation of the bilayer graphene point group. All other processes are strongly suppressed because of destructive interference effects in the Raman amplitude matrix elements. We further show that these dominant ERS processes require isospin flip, i.e. they are chiral Raman-induced electron-hole excitations, and represent only a sub set of the interband transitions of bilayer graphene: interband transitions that are mirror-symmetric with respect to the charge neutral point. These predictions are then tested experimentally by investigating the symmetry resolved ERS continuum in a bilayer graphene device under varying gate voltage. As expected theoretically, the ERS continuum is dominated by interband excitations of  $A_2$  symmetry. They display a characteristic Pauli-blocking behavior upon varying gate voltage, which can be reproduced by taking into account only chiral excitations. This demonstrates that non-chiral excitations make a vanishing contribution to the Raman cross-section, as predicted theoretically. We further contrast this unique property of ERS to infrared absorption measurements, which probe all interband transitions, partially masking the contribution arising from chiral excitations.

## 2. Raman scattering electronic excitations in bilayer graphene: theory

The unit cell of bilayer graphene contains four inequivalent atoms  $A_1$ ,  $B_1$ ,  $A_2$  and  $B_2$ , where letters  $A$  and  $B$  denote two sublattices in the same layer and  $1/2$  stands for the bottom/top layer. The Fermi level in graphene lies in the vicinity of the corners of the hexagonal Brillouin zone (also called valleys) known as  $K_+$  and  $K_-$  [1a]. Due to interlayer coupling, the valence and conduction bands of bilayer graphene split in two subbands.

The conventional tight-binding Hamiltonian is based on  $\pi$ -orbitals of carbon atoms (one per atom, four in the unit cell). We take into account only the in-plane coupling  $\gamma_0$ , the interlayer coupling between dimer atoms  $B_1$  and  $A_2$   $\gamma_1$  and the interlayer coupling between non-dimer orbitals  $A_1$  and  $B_2$   $\gamma_3$ . The main term in the Hamiltonian, linear in momentum  $\mathbf{p}$  around the valleys reads

$$\hat{H}_0 = \begin{pmatrix} \xi v_3(\sigma_x p_x - \sigma_y p_y) & \xi v \boldsymbol{\sigma} \cdot \mathbf{p} \\ \xi v \boldsymbol{\sigma} \cdot \mathbf{p} & \gamma_1 \sigma_x \end{pmatrix}, \quad (1)$$

where  $v = \sqrt{3}a\gamma_0/2\hbar$  is the band velocity and  $v_3 = \sqrt{3}a\gamma_3/2\hbar$ . It results in the low energy electronic bands have a parabolic behavior, that becomes linear at high frequency [see figure 1(a, b)]. Here,  $\boldsymbol{\sigma} = (\sigma_x, \sigma_y)$  and  $\sigma_x, \sigma_y, \sigma_z$  are the Pauli matrices,  $\xi = \pm$  is the valley index. The basis is constructed using components corresponding to atomic sites  $A_1, B_2, A_2, B_1$  in the valley  $K_+$  and  $B_2, A_1, B_1, A_2$  in  $K_-$ . The next order, quadratic in the electron momentum, of the tight-binding Hamiltonian is

$$\delta \hat{H} = \mu \begin{pmatrix} \frac{v_3}{v}[\sigma_x(p_x^2 - p_y^2) + 2\sigma_y p_x p_y] & \sigma_x(p_x^2 - p_y^2) - 2\sigma_y p_x p_y \\ \sigma_x(p_x^2 - p_y^2) - 2\sigma_y p_x p_y & 0 \end{pmatrix}, \quad (2)$$

where  $\mu = -\frac{v^2}{6\gamma_0}$ .

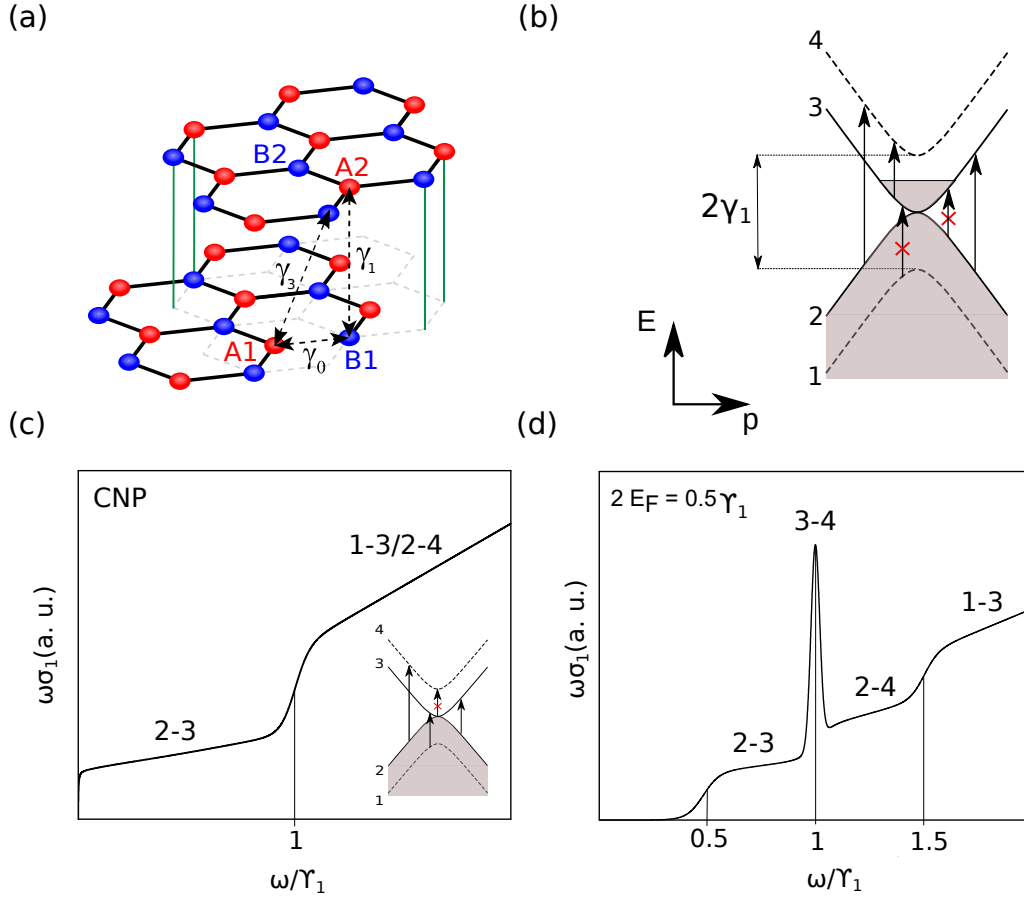


**Figure 1.** (a) Bernal-stacked bilayer graphene. The unit cell defines four non-equivalent sites,  $A_1$ ,  $B_1$ ,  $A_2$  and  $B_2$ . The atoms  $A_2$  and  $B_1$  (dimer atoms) are sitting directly on top of each other. The coupling terms  $\gamma_0$ ,  $\gamma_1$  and  $\gamma_3$  between the atoms are highlighted with arrows. (b) Bilayer graphene electronic bands showing vertical inter-band electron-hole transitions. (c) and (d) Sketch of expected  $\omega\sigma_1$  at the charge neutrality point  $E_F=0$  (c) and with  $2E_F = 1500\text{cm}^{-1}$  (d). In both cases a phenomenological broadening of  $\sim 0.05\gamma_1$  was used to account for disorder and/or inhomogeneous carrier distribution. Here we do not show the  $1-4$  interband excitations, that have an onset energy  $E_{On}^{1-4} = 2\gamma_1 \sim 6000\text{cm}^{-1}$  and are sensitive to the Pauli blocking for  $E_F > \gamma_1$ .

Because of the vanishing small momentum transfer involved in the Raman process with visible photons, the ERS spectrum will be dominated by vertical interband transitions. These vertical transitions are represented in Fig. 1(b) in the band structure of bilayer graphene. For illustrative purposes, we first describe the excitation spectrum ignoring Raman matrix element selection rules (which will be shown to be crucial later) and take into account the energy and momentum conservation rules only. In that case, the ERS spectrum does not depend on photon polarizations and is simply given by the imaginary part of the dynamical electronic polarizability  $\Pi$ , which in turn is closely related to the optical conductivity  $\sigma_1$  by the following relationship  $\Pi'' \propto \omega\sigma_1$  [18, 19]. Figures 1(c) and (d) show the frequency dependence  $\omega\sigma_1$  for bilayer graphene due to

interband transitions, at the charge neutrality point (c) and biased (with  $E_F \neq 0$ ) (d) using the theoretical expression of  $\sigma_1$ , which was shown to give a good description of the infrared absorption spectrum of bilayer graphene [20, 21, 22, 23].

The 2-3 interband transitions have the lowest energy and their spectrum has an onset  $2E_F$ , what makes them analogous to the one observed in monolayer graphene. For  $\gamma_1 > E_F > 0$  the 2-4 interband transitions show an onset at  $\gamma_1$ , and 1-3 transitions are activated from  $\gamma_1 + 2E_F$  on, when the Pauli-blocking is lifted off. On the other hand, the 3-4 transitions do not show an onset, but a peak centered approximately at  $\gamma_1$ , where intensity increases dramatically at finite doping due to increased phase space. This transition was indeed shown to dominate in the infrared absorption spectrum of bilayer graphene samples and devices [21, 24, 23, 22].

### 2.1. Raman processes in bilayer graphene and connection to isospin

In order to define the Raman selection rules, we need to describe the interaction of the electrons with electromagnetic field. To achieve this the canonical momentum should be introduced,  $\mathbf{p} - e(\mathbf{A}_L + \mathbf{A}_S)$ , where  $\mathbf{A}_L$  and  $\mathbf{A}_S$  are the vector potentials of the incoming and outgoing light, respectively. We expand the resulting Hamiltonian up to the second order in the vector potential and write down the interaction part:

$$\hat{H}_{\text{int}} = \mathbf{j} \cdot (\mathbf{A}_L + \mathbf{A}_S) + M_w, \quad \hat{M}_w = \frac{e^2}{2} \sum_{i,j} A_L^i A_S^j \partial_{p_i} \partial_{p_j} \delta \hat{H}, \quad (3)$$

where  $\mathbf{j} = (j_x, j_y)$ ,  $j_i = -e \partial_{p_i} \hat{H}_0$  is the current vertex and  $\hat{M}_w$  is an amplitude of the one-step Raman process. The two-step process is realized through the subsequent absorption/emission processes described by the first term in Eq. (3). Due to the small parameter  $v/c$ , the energy of the intermediate state is of order of the energy of the finite state and is much smaller than the incoming light frequency  $\Omega_L$ , making the intermediate state of the whole system virtual. The virtual absorption process may precede the emission process creating the large excess of energy in the virtual state ( $\approx \Omega_L$ ), or succeed the emission process leading to the large deficit of energy in the virtual state ( $\approx -\Omega_L$ ). Thus, they correspond to zero and two-photon intermediate states respectively.

The two kind of two-step Raman scattering processes are illustrated in Fig. 2(a) and (b). In each figure the absorption (solid lines) and emission (dashed lines) events can take place in any order. Note, however, that swapping the absorption and emission processes (within one figure) we swap also the sequence of the creation and annihilation operators in the initial (i) and finite (f) electronic states. Therefore, each of figures (a) and (b) describes two sequences (with direct and reverse order of absorption and emission events) that constitute the Raman scattering event. The swapping of the photons creation and annihilation operators does not change the expression due to their bosonic nature, while the same swapping for the electrons ladder operators results in the minus sign due to their fermionic statistics. We now calculate explicitly the Raman

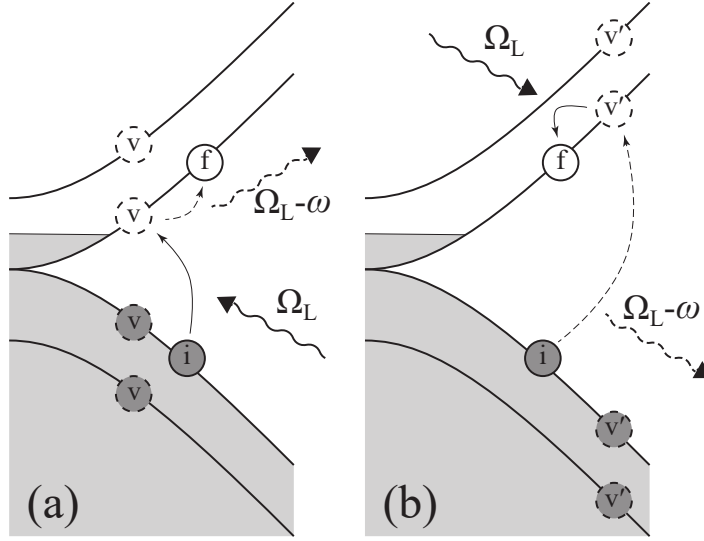


**Figure 2.** Two-step Raman processes in bilayer graphene.  $i$ ,  $v$  and  $f$  correspond to initial, intermediate (virtual) and final electronic states respectively.  $\Omega_L$  is the incoming light frequency and  $\omega$  the Raman shift. The absorption (emission) processes are represented by solid (dashed) lines. They correspond to processes involving zero (a) and two-photon (b) virtual intermediate states

probability of two-step electronic transitions in bilayer graphene. For the two possible sequences in the Fig. 2(a) we get

$$\begin{aligned} \sum_v \left[ a_f^+ a_v \frac{1}{\Omega_L - \epsilon_v + \epsilon_i} a_v^+ a_i + a_v^+ a_i \frac{1}{-(\Omega_L - \omega) - \epsilon_f + \epsilon_v} a_f^+ a_v \right] &= \\ &= \sum_v \left[ \frac{1 - f_v}{\Omega_L - \epsilon_v + \epsilon_i} a_f^+ a_i + \frac{f_v}{-\Omega_L + \epsilon_v - \epsilon_i} a_i a_f^+ \right] = \sum_v \frac{1}{\Omega_L - \epsilon_v + \epsilon_i} a_f^+ a_i, \end{aligned}$$

where index  $v$  denotes all possible (according to the momentum conservation law) virtual states, and  $a$ ,  $a^+$  are fermion destruction and creation operator, respectively. Here we also used the relation  $\epsilon_f = \epsilon_i + \omega$  where  $\omega > 0$  is the Raman shift, i.e. the energy of the electronic excitation created in the system. Similarly, for the Fig. 2(b) we get

$$\begin{aligned} \sum_{v'} \left[ a_{v'}^+ a_i \frac{1}{\Omega_L - \epsilon_f + \epsilon_{v'}} a_f^+ a_{v'} + a_f^+ a_{v'} \frac{1}{-(\Omega_L - \omega) - \epsilon_{v'} + \epsilon_i} a_{v'}^+ a_i \right] &= \\ &= \sum_{v'} \left[ \frac{f_{v'}}{\Omega_L - \epsilon_f + \epsilon_{v'}} a_i a_f^+ + \frac{1 - f_{v'}}{-\Omega_L + \epsilon_f - \epsilon_{v'}} a_f^+ a_i \right] = \sum_{v'} \frac{1}{-\Omega_L - \epsilon_{v'} + \epsilon_f} a_f^+ a_i. \end{aligned}$$

Exploiting the expressions for the current operators, the Raman amplitude of the two-step process then is written as

$$\hat{M}_D = (\mathbf{j} \cdot \mathbf{A}_S) [\Omega_L - H_0 + \epsilon_i]^{-1} (\mathbf{j} \cdot \mathbf{A}_L) + (\mathbf{j} \cdot \mathbf{A}_S) [-\Omega_L + \omega - H_0 + \epsilon_i]^{-1} (\mathbf{j} \cdot \mathbf{A}_L). \quad (4)$$

Because of momentum conservation the components of the Hamiltonian  $H_0$  can be estimated as  $\omega$  or  $\gamma_1$  depending whether the intermediate state in the low or high

energy bands. For typical laser frequency in the visible ( $\sim 2$  eV) we have  $\gamma_1 \ll \Omega_L$ , so for small Raman shift,  $\omega \ll \Omega_L$ , the denominators can be approximated by  $\sim \Omega_L$  and  $\sim -\Omega_L$  for the both kinds of Raman processes. Strong destructive interference effects between the two amplitudes are thus expected to occur if incoming and outgoing photon polarizations are linear and identical. However, as we show below, this is not the case if they are orthogonal.

Expanding over the  $1/\Omega_L$  the Raman amplitudes for the one-step and two-step processes can be estimated as

$$\hat{M}_w \sim \frac{e^2}{\Omega_L} \mu \sim \frac{e^2 v^2}{6\Omega_L \gamma_0}, \quad \hat{M}_D \approx \frac{e^2 v^2}{\Omega_L^2} \{[j_x, j_y] - (\mathbf{e}_L \times \mathbf{e}_S)_z + O[\omega/\Omega_L] + O[\gamma_1/\Omega_L]\}.$$

Here,  $\mathbf{e}_L$  and  $\mathbf{e}_S$  are the polarizations of the incoming and scattered photons. Since  $\gamma_0 \gg \Omega_L$  the one-step term is small and the ERS signal will be dominated by two-step processes. Neglecting also the terms proportional to  $v_3^2$  in the currents commutator ( $v_3/v \sim 0.1$ ) we get

$$\hat{M} \approx \frac{e^2 v^2}{\Omega_L^2} \left\{ \begin{pmatrix} \sigma^z & 0 \\ 0 & \sigma^z \end{pmatrix} (\mathbf{e}_L \times \mathbf{e}_S)_z + O[v_3^2/v^2] + O[\omega/\Omega_L] + O[\gamma_1/\Omega_L] + O[\Omega_L/\gamma_0] \right\}. \quad (5)$$

In our analysis we neglect the momentum of the photon, since the Fermi wavelength for  $E_F = 700\text{cm}^{-1}$  is  $\sim 50\text{nm}$ , what is much less than the laser wavelength  $\sim 500\text{nm}$ . The resulting Raman amplitude is dominated by processes in which incoming and outgoing photon polarizations are orthogonal. In terms of the symmetry representation of the point group of graphene, the scattering processes correspond to  $A_2$  symmetry representation [25]. As discussed above, this Raman selectivity can be traced back to the destructive interference effects between the two kinds of two-step processes shown in figure 2.

Interestingly, the dominant  $A_2$  symmetric Raman amplitude has a simple connection with the isospin, which in 4-bands model is defined in the basis of the Hamiltonian (1) as

$$\mathbf{S} = \sigma^0 \otimes \boldsymbol{\sigma} \equiv \begin{pmatrix} \boldsymbol{\sigma} & 0 \\ 0 & \boldsymbol{\sigma} \end{pmatrix}, \quad \boldsymbol{\sigma} = (\sigma^x, \sigma^y, \sigma^z), \quad (6)$$

where  $\sigma^0$  is a unity matrix. This definition is equivalent to the spin definition in the 2-bands model given in Refs. [26, 27]. As one can see, the dominant  $A_2$  Raman amplitude is proportional to the  $z$  component of the isospin and can be written as  $\hat{M} = \frac{e^2 v^2}{\Omega_L^2} (\mathbf{e}_L \times \mathbf{e}_S)_z S^z$ .

## 2.2. Symmetry of excitations and relation to chirality

We have shown that the dominant Raman processes have  $A_2$  symmetry and transforms like the  $z$  component of the isospin, and now investigate to which interband transitions they correspond to. For this we analyze the structure of the general solution of the Hamiltonian (1), and demonstrate that the dominant Raman process are excitations between bands symmetric with respect to the  $E = 0$  line, i.e. from band 3 to 2 and

from 4 to 1 only. We further show that they correspond to inversion of the isospin orientation, and are thus chiral.

Let us consider the structure of the eigenstates of the Hamiltonian (1) in the new basis  $A1, A2, B2, B1$ . The Hamiltonian  $H_0$  then takes form

$$H_0 = \begin{pmatrix} 0 & h \\ h^* & 0 \end{pmatrix}, \quad h = \begin{pmatrix} v_3 \mathbf{p}^* & v \mathbf{p} \\ v \mathbf{p} & \gamma_1 \end{pmatrix},$$

where  $\mathbf{p} = p_x + ip_y$ . The solutions of the Schrödinger equation  $H_0|\psi\rangle = E|\psi\rangle$  are represented by eigenvectors

$$|\pm, a/b\rangle = \frac{1}{\sqrt{2}} \begin{pmatrix} |a/b\rangle \\ \pm \lambda_{a/b}^{-1/2} h^* |a/b\rangle \end{pmatrix}, \quad hh^* |a/b\rangle = \lambda_{a/b} |a/b\rangle, \quad (7)$$

with eigenvalues  $E = \pm \sqrt{\lambda_{a/b}}$  such that  $|a/b\rangle$  and  $\lambda_{a/b}$  are eigenvectors and eigenvalues of the matrix  $hh^*$ , correspondingly. Note that  $\lambda_{a/b}$  are real and positive. The eigenstates we found here coincide with the bilayer bands as  $|-, a\rangle \equiv |1\rangle$ ,  $|-, b\rangle \equiv |2\rangle$ ,  $|+, b\rangle \equiv |3\rangle$ , and  $|+, a\rangle \equiv |4\rangle$ . In the new basis the isospin and Raman amplitude (in the limit of Eq. (5)) are equal to

$$\mathbf{S} = \boldsymbol{\sigma} \otimes \sigma^0, \quad \hat{M} \propto S^z \equiv \begin{pmatrix} \sigma^0 & 0 \\ 0 & -\sigma^0 \end{pmatrix}. \quad (8)$$

Since all eigenvectors are orthogonal, the Raman amplitude  $\hat{M} \propto S^z$  couples the states with the opposite sign of the energy

$$S^z |\pm, a/b\rangle = |\mp, a/b\rangle. \quad (9)$$

This also means that the expectation value of the isospin vector  $\langle n | \mathbf{S} | n \rangle$  lies in the graphene's plane, since the  $z$ -component of its the expectation value is zero. In terms of the band transitions shown in Fig. 1(b), the dominant Raman scattering process invokes the transitions  $1 \rightarrow 4$  and  $2 \rightarrow 3$  only. All other transitions have vanishingly small Raman amplitude as described above. The anticommutation relation  $MS^{x/y} = -S^{x/y}M$  manifests that the initial and final electronic states involved in the Raman process (see Fig. 2) have the same momentum, but possess opposite isospins, and thus opposite signs of the spin projection onto momentum, i.e. opposite chirality in graphene's language.

### 3. Electronic Raman scattering in bilayer graphene: experiments

Armed with the preceding theoretical predictions, we now test them experimentally in a bilayer graphene device. Our objective is two-fold: to show that the dominant Raman processes have  $A_2$  symmetry, and test whether they can be ascribed to  $2 \rightarrow 3$  interband transitions at low energy. This will establish Raman scattering as a selective probe of chiral excitations in graphene systems.

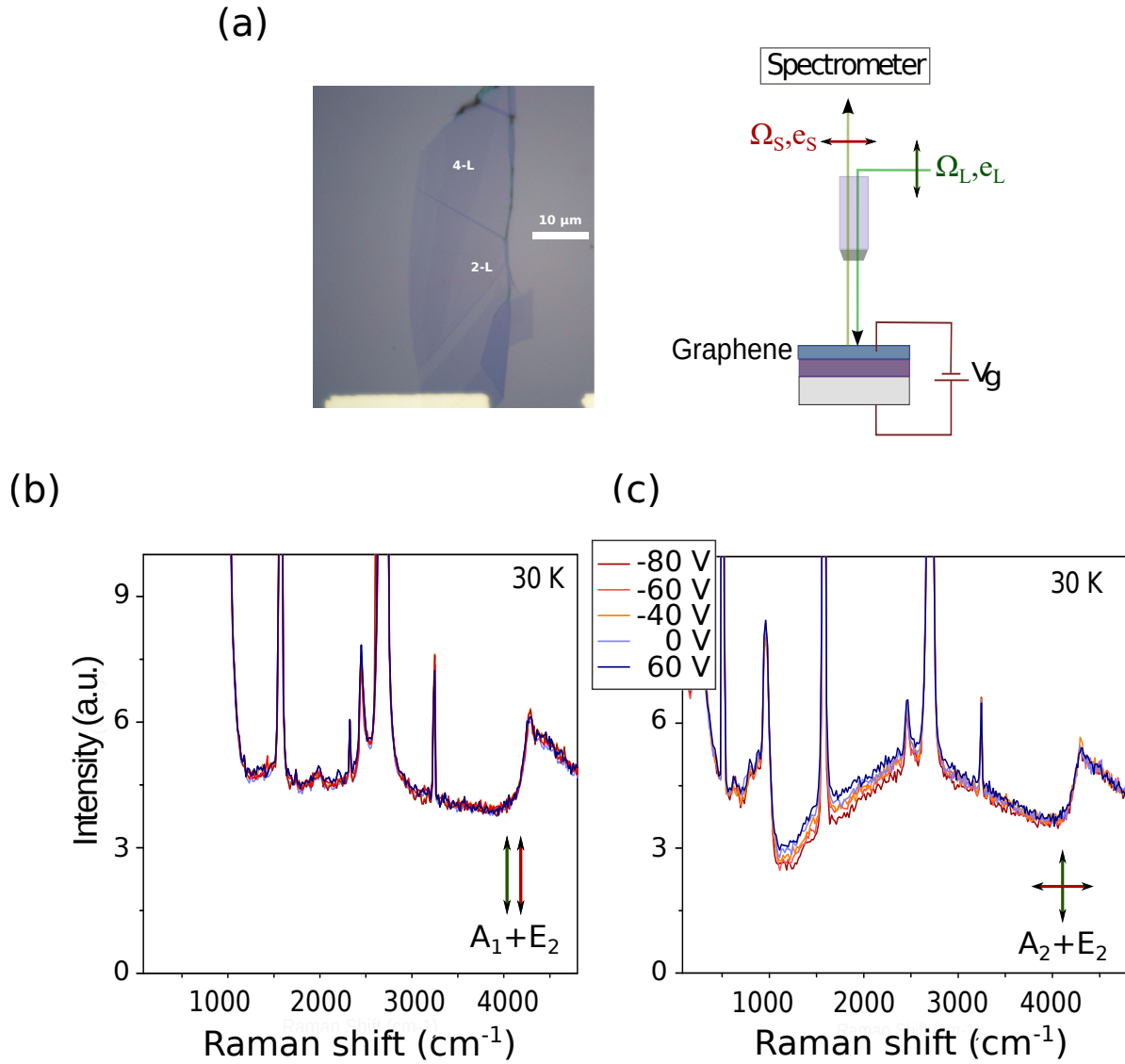


**Figure 3.** (a) Optical microscope image of bilayer graphene device, and schematic drawing of the set-up.  $\epsilon_{L,S}$  and  $\Omega_{L,S}$  are the frequencies and polarizations of incoming and scattered photons. The Raman shift is defined as  $\omega = \Omega_L - \Omega_S$ . (b) and (c) Polarization resolved Raman continuum of bilayer graphene recorded at  $T = 30\text{K}$  at five different gate voltage values for parallel (a) and cross (b) polarizations of incoming and scattered photons.

### 3.1. Methods

The graphene samples studied were produced by exfoliation of natural graphite and first characterized by phononic Raman spectroscopy. The study of 2D band ( $\sim 2600\text{ cm}^{-1}$ ) and M band ( $1700\text{-}1800\text{ cm}^{-1}$ ) features allowed to identify unambiguously the sample thickness, following [28]. The sample shown in figure 3(a) consists of a bilayer and quadrilayer Bernal-stacked graphene. Electrical contacts were first fabricated using e-beam lithography and Pd deposition on an oxidized Si wafer ( $\text{SiO}_2 \sim 500\text{nm}$ ).

The graphene flake was then positioned using a dry transfer technique on the top

of the  $Si/SiO_2$  device. In such a structure the doped  $Si$  substrate acts as a back gate [see Fig. 3(a)]. The use of a back gate is crucial in order to isolate the ERS continuum from the other sources of continuum background in the measured spectra. The graphene device was first characterized by studying the gate voltage evolution of the G band phonon energy and linewidth. The charge neutrality point corresponding to zero Fermi energy,  $E_F = 0$ , was found by symmetry at  $50 \pm 10$  V. The polarization resolved Raman scattering measurements were performed using a home-built micro-Raman set-up in a back-scattering configuration. The  $\lambda = 532nm$  ( $2.33$  eV) excitation line of a Diode Pumped Solid State (DPSS) Laser was focused onto the sample using a long working distance 100X objective lens with N.A.=0.8. The laser spot was  $\leq 1\mu m$  and all measurements were performed with an incident laser power less than  $1$  mW. The measurements were performed in the vacuum chamber ( $P \leq 10^{-5}mbar$ ) of a low temperature optical cryostat. The lowest cold finger temperature achieved was  $\sim 30K$ . The excitation beam and the collected signal were linearly polarized in order to identify the symmetry of the Raman active excitations.

### *3.2. Gate dependent electronic Raman spectrum of bilayer graphene*

Figures 3(b) and (c) show Raman continuum of bilayer graphene recorded at  $T = 30K$  as a function of the applied gate voltage, in parallel (b) and cross (c) polarizations which probe all excitations belonging to  $A_1 + E_2$  and  $A_2 + E_2$  symmetry representations of bilayer graphene, respectively [15]. The spectra exhibit sharp peaks corresponding to the well-known Raman active optical phonons of graphene layers. Here we focus on the underlying broad continuum, which partly originate from the ERS processes. In parallel polarization configuration, the Raman continuum does not show any sign of gate dependence, indicating that it likely arises from non-ERS background, or resonant higher order ERS processes [29], as found in monolayer device [15]. On the other hand, the cross polarizations spectra exhibit a clear gate effect, as expected for non-resonant ERS signal coming from low energy interband excitations, with a gradual and partial suppression of intensity as the gate voltage increases [30, 29]. The fact that the gate dependent signal is only seen in cross-polarization indicates a dominant contribution to the ERS continuum from electronic excitations having  $A_2$  symmetry representation as expected theoretically above. Note that the  $A_2$  symmetry gate dependent signal represents at least 20 % of the total intensity in this configuration. As we will show below, the partial suppression of the  $A_2$  ERS continuum upon increasing gate voltage is well-reproduced by considering the Pauli blocking effects on the chiral  $2-3$  inter-band transitions.

In order to isolate the gate dependent ERS signal, we have subtracted the phonon peaks and normalized the resulting spectra with the one recorded at the estimated charge neutrality voltage ( $E_F = 0$ ). The gate dependent signal can then be discussed

in terms of the ratio  $R(\omega, V_G)$  :

$$R(\omega, V_G) = \frac{I(\omega, V_G)}{I(\omega, V_{CN})} = \frac{I_0 + I_{ERS}(\omega, V_G)}{I_0 + I_{ERS}(\omega, V_{CN})} \quad (10)$$

Here  $I_{ERS}(\omega, V_G)$  is the gate dependent ERS bilayer continuum intensity and  $I_0$  the gate independent background signal which we assumed to be weakly frequency dependent. In figure 4(a) we show  $R$  for several gate voltage values. When the Fermi energy is moved away from charge neutrality, the ratio  $R$  decreases and the onset energy of this suppression gradually shifts at higher frequencies, as expected due to Pauli blocking effects.

### 3.3. Theoretical modeling of the spectra

To analyze the gate dependent ERS signal we compute the expected theoretical  $R$  profiles. We only take into account the Raman signal coming from the 2-3 transitions since, as shown theoretically above, they are expected to dominate the ERS spectrum at low Raman shift,  $\omega < 2\gamma_1$ . In this case, the ERS intensity can be analytically computed by using the expression of the Raman amplitude  $\hat{M}$  and the Fermi golden rule. Extending the results of Ref. [30] to finite temperature and taking into-account the deviations from non-parabolicity, we obtain the following frequency dependence:

$$I_{ERS}^{2-3} \propto \frac{\omega + \gamma_1}{\pi(\hbar v_F)^2} \left[ f\left(-\frac{\hbar\omega}{2}\right) - f\left(\frac{\hbar\omega}{2}\right) \right] \quad (11)$$

where  $f(\epsilon) = [1 + e^{\frac{\epsilon - E_F}{k_B T}}]^{-1}$  is the Fermi Dirac distribution. Note that in the low energy or parabolic limit,  $\omega \ll \gamma_1$ , we recover the constant ERS continuum found in [30]. The adjustable parameters in this simple model are  $E_F$ ,  $\delta E_F$ , a distribution of Fermi energy due to the inhomogeneous charge doping, and  $I_0$  an additional constant describing a energy independent background. Figure 4(a) shows the superposition of experimental and theoretical ratios  $R$  demonstrating a good agreement with theoretical expectations. In particular, as shown in figure 4(b), the  $E_F$  values used for the fits (black dots) are very close to the one expected by using the relationship between the Fermi energy  $E_F$  and the charge density  $N$  deduced from the gate voltage and the estimated device capacitance  $C \sim 60 \text{ aF}/\mu\text{m}^2$ :

$$E_F = \frac{-\gamma_1 + \sqrt{\gamma_1^2 + 4\pi N(\hbar v_F)^2}}{2} \quad (12)$$

The Fermi energy distribution assumed for the theoretical curves is  $\delta E = 35 \text{ meV}$ , consistent with previous estimations for bilayer graphene device [31]. Moreover, it is consistent with the energy distribution coming from the fits performed on the gate evolution of the G band in the same device (see below).

### 3.4. Link with G band renormalization

The fitting parameters used for the ERS spectrum can be independently cross-checked by looking at the G band renormalization under gate voltage. The coupling between

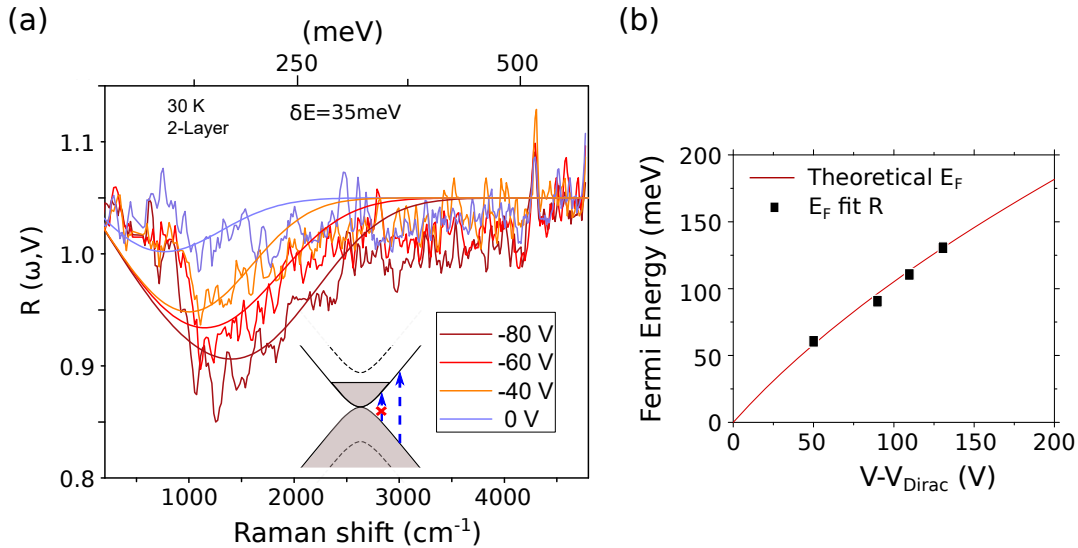


**Figure 4.** (a) Experimental and theoretical  $R(\omega, V_G)$  at 30 K for the cross polarizations spectra. The theoretical plots are obtained by only considering vertical 2-3 interband transitions, with a Gaussian distribution of Fermi energy with  $\delta E_F \sim 35 \text{ meV}$ . (b) Adjusted values of  $E_F$  in function of the gate voltage, superposed to the theoretical curve 12.

phonons and low energy electrons pairs in graphene devices has been studied both theoretically [32, 33, 34] and experimentally [35, 36, 31]. Figure 5(a) shows the G band energy and width as a function of the Fermi energy shifts in our device. When the Fermi energy crosses half of the phonon frequency ( $E_F = \pm \hbar \omega_G / 2$ ), the G band energy displays an anomalous softening and its linewidth drops sharply [31]. In experimental measurements, the profile of this anomaly strongly depends on the inhomogeneous charge distribution, which is then a crucial parameter in order to correctly reproduce the anomaly. In our case the value of the distribution of Fermi energy  $\delta E_F$  assumed for the fit of  $R$  is perfectly consistent with the one coming from the G band energy and linewidth renormalizations.

In addition, we also note that the linewidth renormalization of the G band is directly linked to the vertical electron-hole pairs excitations at  $\omega_G$  [32, 33]. At this energy only 2-3 transitions are allowed and they have mainly chiral  $A_2$  character, as already discussed for the ERS spectra. As such they should not couple to the G band phonon, which has  $E_2$  symmetry. However, taking into account trigonal warping  $v_3$  the 2-3 vertical interband transitions acquire a small but finite  $E_2$  component which allows coupling to the G band, as discussed by e.g. Basko [37]. The superposition of the ERS intensity taken at  $\omega \sim 1580 \text{ cm}^{-1}$ , and the G band linewidth at several values of the Fermi energy, is shown in figure 5(b). The similar evolutions of the two quantities indicate they are indeed both linked to 2-3 interband transitions.

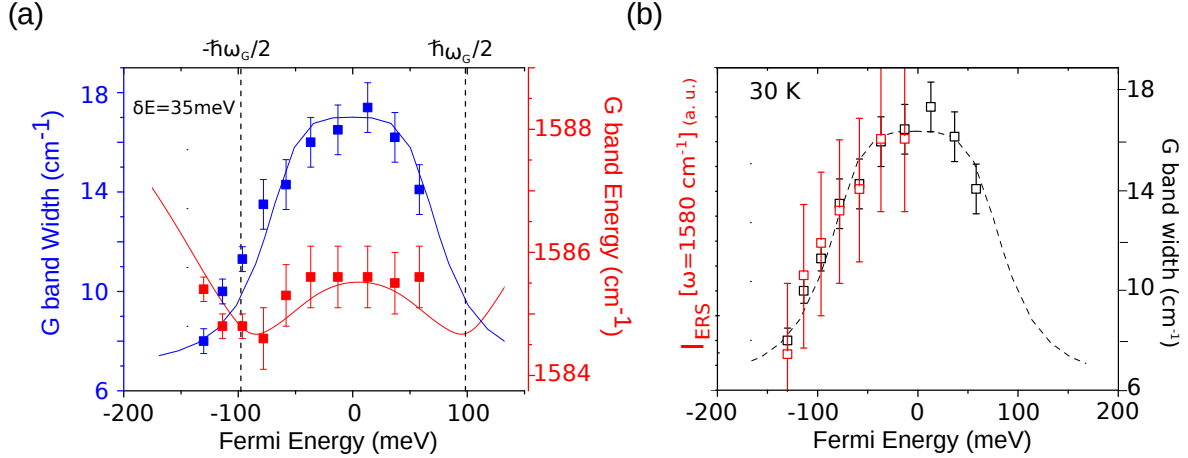


**Figure 5.** (a) Evolution of G band linewidth (blue dots) and energy (red dots) of the bilayer graphene sample as a function of Fermi energy. The Fermi energy was deduced from the gate voltage using the same device capacitance as in the case of the ERS spectra. Theoretical plots are obtained with a distribution of Fermi energy with  $\delta E_F \sim 35 \text{ meV}$  according to the  $R(\omega, V_G)$  theoretical lines (see Fig 4 (c)). One of the two anomalies is clearly identified at  $E_F = -\hbar\omega_G/2$ . (b) Evolution of the ERS intensity at  $1580 \text{ cm}^{-1}$  (red dots) and of the G band linewidth (black dots) as a function of the Fermi energy, and theoretical expectation (dotted line).

### 3.5. Contrast between optical conductivity and ERS in bilayer graphene

We now discuss the specificity of ERS as a selective probe of chiral excitations, and in particular the striking contrast between ERS and infrared transmission and reflectivity measurements in bilayer graphene. Unlike in the monolayer graphene case, the difference between optical conductivity and Raman response of bilayer graphene is substantial. In monolayer graphene only one vertical interband transition is possible and selection rules play a marginal role. In that case ERS and optical conductivity yield essentially the same information and are related via a simple relation,  $I_{ERS} = \omega\sigma_1$ . As shown above, the ERS spectrum of bilayer graphene is well reproduced by taking into account only the  $A_2$  chiral transitions between the bands 2 and 3, essentially neglecting all other interband transitions. By contrast, all interband transitions contribute to optical conductivity. Figure 6 illustrates the striking difference of ERS and infrared transmission measurements for the case of bilayer graphene. It shows a superposition of  $R(\omega, V_G)$  at  $-40 \text{ V}$  and a normalized infrared transmission data taken from [23], which we used as a proxy for the optical conductivity of bilayer graphene. Both set of data were taken on a bilayer graphene device with a comparable Fermi energies,  $E_F \sim 95 \text{ meV}$ . The infrared spectrum is dominated by a peak at  $\sim 3000 \text{ cm}^{-1}$  arising from non-chiral  $3-4$  transitions at  $\gamma_1$  as expected from the theoretical optical conductivity. This prominent peak is masking the broader contribution from  $2-3$  chiral transitions in the infrared spectrum. By contrast the peak at  $\gamma_1$  is essentially absent in the ERS spectrum confirming that non-chiral excitations are filtered out in the ERS process.

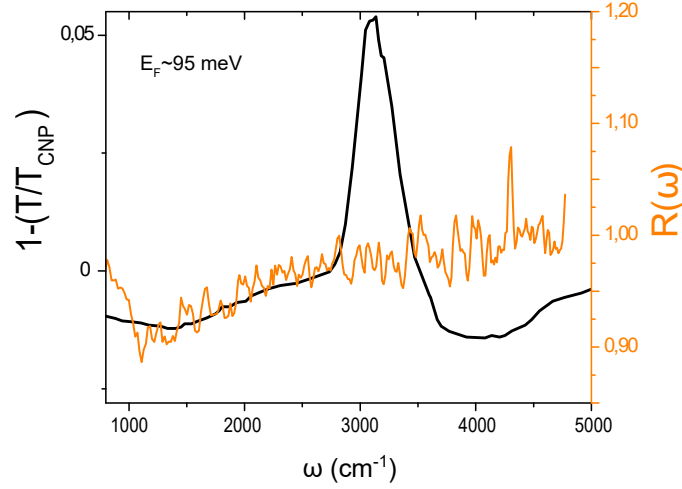


**Figure 6.** Comparison of  $R(\omega, V_G)$  with normalized infrared transmission measurements  $(1 - T/T_{CN})$  where  $T_{CN}$  is the transmission for a Fermi energy at the charge neutrality point. Both were performed on bilayer graphene devices [23] with approximately the same Fermi level shift. The  $1 - (T(V)/T_{CN})$  spectra are dominated by a peak at around  $3000 \text{ cm}^{-1}$ , with a magnitude that increases systematically with gate voltage. By contrast the ERS intensity at this frequency is essentially independent of gate voltage.

#### 4. Conclusion

In this paper we have presented the first electronic Raman scattering study of a bilayer graphene sample under gate voltage. The spectra show a remarkable selectivity of the Raman probe on the inter-band excitations that inverse the electron chirality. Theoretically this selectivity is ascribed to the fact that the dominant electronic Raman processes of bilayer graphene belong to the  $A_2$  symmetry, which includes only chiral electronic transitions. Processes in other symmetry are shown to be suppressed due to strong destructive interferences effects in the Raman amplitudes. This selectivity contrasts with infrared transmission measurements and opens interesting venues for the use of Raman scattering as a selective probe of isospin and chiral degrees of freedom in topological matter and other 2D crystals.

##### *Appendix .1. Chirality, helicity, and spin-momentum locking*

In our work we use the terminology accepted by the graphene community referring to the spin-momentum locking phenomenon as chirality [26, 4, 5, 27]. Nevertheless, it is important to introduce clearer definitions, in order to clarify which properties we probe in the experiment. The chiral excitations, by definition, are the solutions of the Hamiltonian, for which the parity transformation (a flip in the sign on *one* spatial coordinate, which is equivalent to a reflection through a line in 2D, and through a plane in 3D) cannot be compensated by a rotation [38]. The valleys in monolayer graphene

play a crucial role in making the excitations chiral, since the reflexion exchanges the the K and K' points. To compare with the high-energy physics models, the solutions of the 2D Dirac Hamiltonian  $\boldsymbol{\sigma} \cdot \mathbf{p}$  constructed by means of  $2 \times 2$  Pauli matrices  $\sigma$  are non-chiral. Meanwhile, the same Hamiltonian in 3D (with extra term  $\sigma^z p_z$ ), contains only chiral solutions, since it itself is not symmetric with respect to the parity (which in 3D is equivalent to inversion—the flipping in the sign of all three spatial coordinates). The chirality of monolayer graphene excitations is preserved also at higher energies where the trigonal warping is relevant and the rotations degrade from SO(2) to C<sub>6</sub>. These statements about chirality are also correct for bilayer graphene.

If one follows the particle physics terminology, the spin-momentum locking property of monolayer graphene referred to in graphene community as chirality is actually called *helicity* [38], which is defined as the projection of the angular momentum or spin onto the direction of momentum. Indeed, the helicity of the state in the monolayer graphene takes the discrete values of +1 and -1 denoting also the band which this state belongs to. In case of the bilayer graphene this simple definition fails. For the particular case of low-energy excitations in bilayer graphene, the Ref. [27] defines helicity as  $\boldsymbol{\sigma} \cdot (p_x^2 - p_y^2, 2p_x p_y)/p^2$ . In case of the four-bands model of bilayer graphene this definition can be generalized, defining helicity as a *continuous* map of the momentum direction onto the iso-spin direction.

As we stated above, in the Raman scattering process the momentum of the excitation is kept fixed, but its isospin direction is changed to the opposite one. The excitation changes the band crossing to the state which is mirror-symmetric with the respect to the  $E = 0$  line. Thus, the electron and hole states of the Raman-induced pair have the opposite projections of the isospin onto momentum. This meets the definition of the term Raman chiral excitations if we use the terminology of the graphene community.

## References

- [1] MI Katsnelson, KS Novoselov, and AK Geim. Chiral tunnelling and the Klein paradox in graphene. *Nature Physics*, 2(9):620, 2006.
- [2] Gordon W Semenoff. Condensed-matter simulation of a three-dimensional anomaly. *Physical Review Letters*, 53(26):2449, 1984.
- [3] F Duncan M Haldane. Model for a quantum hall effect without Landau levels: Condensed-matter realization of the "parity anomaly". *Physical Review Letters*, 61(18):2015, 1988.
- [4] Edward McCann. Asymmetry gap in the electronic band structure of bilayer graphene. *Physical Review B*, 74(16):161403, 2006.
- [5] Edward McCann and Vladimir I Fal'ko. Landau-level degeneracy and quantum hall effect in a graphite bilayer. *Physical Review Letters*, 96(8):086805, 2006.
- [6] Edward McCann and Mikito Koshino. The electronic properties of bilayer graphene. *Reports on Progress in Physics*, 76(5):056503, 2013.
- [7] M Zahid Hasan and Charles L Kane. Colloquium: topological insulators. *Reviews of Modern Physics*, 82(4):3045, 2010.
- [8] Yuqi Xia, Dong Qian, David Hsieh, L Wray, Arijet Pal, Hsin Lin, Arun Bansil, DHYS Grauer, Yew San Hor, Robert Joseph Cava, et al. Observation of a large-gap topological-insulator class with a single Dirac cone on the surface. *Nature Physics*, 5(6):398–402, 2009.

- [9] David Hsieh, Yuqi Xia, Dong Qian, L Wray, JH Dil, F Meier, J Osterwalder, L Patthey, JG Checkelsky, NP Ong, et al. A tunable topological insulator in the spin helical dirac transport regime. *Nature*, 460(7259):1101–1105, 2009.
- [10] Su-Yang Xu, Y Xia, LA Wray, S Jia, F Meier, JH Dil, J Osterwalder, B Slomski, A Bansil, H Lin, et al. Topological phase transition and texture inversion in a tunable topological insulator. *Science*, 332(6029):560–564, 2011.
- [11] H-H Kung, S Maiti, X Wang, S-W Cheong, DL Maslov, and G Blumberg. Chiral spin mode on the surface of a topological insulator. *Physical Review Letters*, 119(13):136802, 2017.
- [12] Stéphane Berciaud, Marek Potemski, and Clément Faugeras. Probing electronic excitations in mono-to-pentalayer graphene by micro magneto-raman spectroscopy. *Nano Letters*, 14(8):4548–4553, 2014.
- [13] Clément Faugeras, Mario Amado, Piotr Kossacki, Milan Orlita, Matthias Kühne, AAL Nicolet, Yu I Latyshev, and Marek Potemski. Magneto-raman scattering of graphene on graphite: Electronic and phonon excitations. *Physical Review Letters*, 107(3):036807, 2011.
- [14] C Faugeras, S Berciaud, P Leszczynski, Y Henni, K Nogajewski, M Orlita, T Taniguchi, K Watanabe, C Forsythe, Philip Kim, et al. Landau level spectroscopy of electron-electron interactions in graphene. *Physical Review Letters*, 114(12):126804, 2015.
- [15] E Riccardi, M-A Méasson, M Cazayous, A Sacuto, and Y Gallais. Gate-dependent electronic raman scattering in graphene. *Physical Review Letters*, 116(6):066805, 2016.
- [16] Oleksiy Kashuba and Vladimir I Fal’ko. Signature of electronic excitations in the raman spectrum of graphene. *Physical Review B*, 80(24):241404, 2009.
- [17] DN Basov, MM Fogler, A Lanzara, Feng Wang, Yuanbo Zhang, et al. Colloquium: graphene spectroscopy. *Reviews of Modern Physics*, 86(3):959, 2014.
- [18] B Sriram Shastry and Boris I Shraiman. Theory of raman scattering in mott-hubbard systems. *Physical Review Letters*, 65(8):1068, 1990.
- [19] Adolfo G Grushin, Belén Valenzuela, and María AH Vozmediano. Effect of coulomb interactions on the optical properties of doped graphene. *Physical Review B*, 80(15):155417, 2009.
- [20] DSL Abergel and Vladimir I Fal’ko. Optical and magneto-optical far-infrared properties of bilayer graphene. *Physical Review B*, 75(15):155430, 2007.
- [21] LM Zhang, ZQ Li, Dimitri N Basov, MM Fogler, Zhao Hao, and Michael C Martin. Determination of the electronic structure of bilayer graphene from infrared spectroscopy. *Physical Review B*, 78(23):235408, 2008.
- [22] AB Kuzmenko, Erik Van Heumen, Dirk Van Der Marel, Philippe Lerch, Peter Blake, KS Novoselov, and AK Geim. Infrared spectroscopy of electronic bands in bilayer graphene. *Physical Review B*, 79(11):115441, 2009.
- [23] ZQ Li, EA Henriksen, Zhigang Jiang, Zhao Hao, Michael C Martin, P Kim, HL Stormer, and Dimitri N Basov. Band structure asymmetry of bilayer graphene revealed by infrared spectroscopy. *Physical Review Letters*, 102(3):037403, 2009.
- [24] Feng Wang, Yuanbo Zhang, Chuanshan Tian, Caglar Girit, Alex Zettl, Michael Crommie, and Y Ron Shen. Gate-variable optical transitions in graphene. *Science*, 320(5873):206–209, 2008.
- [25] Oleksiy Kashuba and Vladimir I Fal’ko. Role of electronic excitations in magneto-raman spectra of graphene. *New Journal of Physics*, 14(10):105016, 2012.
- [26] Edward McCann. Electronic properties of monolayer and bilayer graphene. In *Graphene Nanoelectronics*, pages 237–275. Springer, 2011.
- [27] Kostya S Novoselov, Edward McCann, SV Morozov, Vladimir I Fal’ko, MI Katsnelson, U Zeitler, D Jiang, F Schedin, and AK Geim. Unconventional quantum hall effect and berry’s phase of  $2\pi$  in bilayer graphene. *Nature Physics*, 2(3):177, 2006.
- [28] The An Nguyen, Jae-Ung Lee, Duhee Yoon, and Hyeonsik Cheong. Excitation energy dependent raman signatures of aba-and abc-stacked few-layer graphene. *Scientific Reports*, 4, 2014.
- [29] Eddwi H Hasdeo, Ahmad RT Nugraha, Mildred S Dresselhaus, and Riichiro Saito. Breit-wigner-fano line shapes in raman spectra of graphene. *Physical Review B*, 90(24):245140, 2014.

- [30] Marcin Mucha-Kruczyński, Oleksiy Kashuba, and Vladimir I Fal'ko. Spectral features due to inter-landau-level transitions in the raman spectrum of bilayer graphene. *Physical Review B*, 82(4):045405, 2010.
- [31] Jun Yan, Erik A Henriksen, Philip Kim, and Aron Pinczuk. Observation of anomalous phonon softening in bilayer graphene. *Physical Review Letters*, 101(13):136804, 2008.
- [32] Tsuneya Ando. Anomaly of optical phonon in monolayer graphene. *Journal of the Physical Society of Japan*, 75(12):124701–124701, 2006.
- [33] Tsuneya Ando. Anomaly of optical phonons in bilayer graphene. *Journal of the Physical Society of Japan*, 76(10):104711, 2007.
- [34] AH Castro Neto and Francisco Guinea. Electron-phonon coupling and raman spectroscopy in graphene. *Physical Review B*, 75(4):045404, 2007.
- [35] Simone Pisana, Michele Lazzeri, Cinzia Casiraghi, Kostya S Novoselov, Andre K Geim, Andrea C Ferrari, and Francesco Mauri. Breakdown of the adiabatic born–oppenheimer approximation in graphene. *Nature Materials*, 6(3):198, 2007.
- [36] Jun Yan, Yuanbo Zhang, Philip Kim, and Aron Pinczuk. Electric field effect tuning of electron-phonon coupling in graphene. *Physical Review Letters*, 98(16):166802, 2007.
- [37] Denis M Basko. Theory of resonant multiphonon raman scattering in graphene. *Physical Review B*, 78(12):125418, 2008.
- [38] Michael E Peskin and Daniel V Schroeder. An introduction to quantum field theory (boulder, co, 1995.